From Joel S. Levine, BIOMASS BURNING AND GLOBAL CHANGE, Volume 2, (Cambridge, MA: The MIT Press 1996) pp. 697-715.

Particle and Trace-Gas Measurements in the Smoke from Prescribed Burns of Forest Products in the Pacific Northwest

Peter V. Hobbs, Jeffrey S. Reid, John A. Herring, J. David Nance, Ray E. Weiss, John L. Ross, Dean A. Hegg, Roger D. Ottmar, and Catherine Liousse

We describe here the results of airborne in situ and airborne remote-sensing measurements of the smoke from three prescribed burns of forest products in the Pacific Northwest. The studies were carried out as part of the *Smoke, Clouds and Radiation-C (SCAR-C) Project*. This project was unique in that it included careful characterization from the ground of the nature and consumption rates of the fuels and fire behavior, airborne in situ and remote-sensing measurements of particles and gases in the smoke (from the University of Washington's Convair C-131A research aircraft), and remote-sensing measurements (from NASA's high-flying ER-2 research aircraft). The three prescribed burns described here (the Quinault, Creamery, and Raymond burns) are typical of large, clearcut, prescribed burns that occur periodically along the coastal forest lands of the Pacific Northwest. They were selected to cover a range of fuel loading, unit sizes, and burning conditions. This paper primarily deals with measurements obtained from the Convair C-131A aircraft and their relationships to the burns. Other aspects of SCAR-C are described elsewhere in this book.

Nature of the Prescribed Burns and Ground-Based Measurements

To illustrate the types of airborne measurements and results obtained in this study, we use data primarily from the Quinault burn. However, comparisons are made with the Creamery and Raymond burns.

Quinault Prescribed Burn

The Quinault burn was a 19.4-hectare (ha) clearcut unit on the Pacific coast of Washington State on the Quinault Indian Reservation (figure 66.1). The fuel consisted of old-growth large western red cedar debris left over from logging that occurred early in the 1900s. Nearly 262 Mg (262×10^6 g) per hectare of woody residue were on the site before the burn. The forest floor was deep (7.1 cm) and fuel loading was estimated at 117.5 Mg/ha. The moisture content of the fuel was estimated at 25%. Total fuel consumption was about 217.3 Mg/ha. Table 66.1 provides further information on fuel loadings, consumption, and moisture.

The prescribed burn took place on 21 September 1994. Ignition, which started at about 1105 PDT and was rapid (~40 min.), was by helicopter, using a suspending ignition device called Helitorch. The other two burns described below were ignited by the same technique.

The burn site was divided into ten subunits (figure 66.2*a*). A forester, situated at a vantage point, noted the time as each subunit was ignited, the time it took for each subunit to be fully engulfed in flaming combustion, the time it took each subunit to be transformed into smoldering combustion, and the length of time smoldering continued.

Although the Quinault site held a large loading of cedar debris and was ignited from a helicopter in approximately 40 minutes, the flat terrain and large size of the logs slowed the progression of the heat release and the buildup of emission products (figure 66.3). Estimates from ground observations of the plume and ignition pattern indicated the maximum heat-release rate probably occurred between 1215 and 1245 PDT, when maximum acres were in combustion. The unit was entirely in the smoldering stage at 1300 PDT. The large logs, deep forest floor, and relatively low fuel-moisture content continued to smolder for 6 to 7 h after ignition. The total duration of the fire was about 9 h.

Figure 66.3 shows plots of the progression of the ignition (steep positive slope in graph), the flaming stage of combustion (flat portion of graph), and the smoldering phase (exponential downward-sloping curve) for each of the ten subunits in the Quinault burn. The heat-release rate and the PM 2.5 (i.e., particles in smoke with diameters $\leq 2.5\mu$m) mass-production rate over time for the Quinault burn, estimated using the emissions production model of Sandberg and Peterson (1984), are shown in figures 66.4 and 66.5.

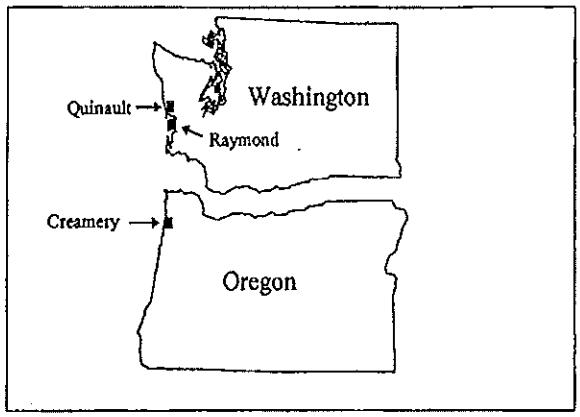

Figure 66.1 Locations of the three prescribed burns

Creamery Prescribed Burn

The Creamery prescribed burn, which occurred on 22 September 1994, was a 44.5-ha clearcut unit east of Tillamook, Oregon, on private timberlands (see figure 66.1). Loadings of the woody fuels (primarily Douglas fir/hemlock) were typical of second-growth logged areas west of the Cascade Mountains in the Pacific Northwest. Woody fuel loadings were estimated at 62.6 Mg/ha. Organic layers of the forest floor were relatively shallow. Forest-floor loading was 41.9 Mg/ha (2.5 cm in depth). The fuel moisture content of the large logs was estimated to be 28%. Total fuel consumption was estimated to be 61.1 Mg/ha. More detailed information is given in table 66.1.

The subunits 1 to 9 of the Creamery prescribed burn were ignited from a helicopter in approximately 30 min., between 1130 and 1200 h PDT (figure 66.6). Due to mechanical problems with the helicopter, subunit 10 was ignited 2.5 h later. The homogeneous small woody fuel bed and steep slopes allowed quicker progression to maximum heat release and emissions production than for the Quinault burn. Ground observation of the plume and lighting indicated that the maximum heat release rate probably occurred between 1200 and 1230 PDT. The entire site was smoldering by 1230 PDT. Because the woody fuel moisture content was lower, and there was less large woody debris and forest floor material than on the Quinault site, the smoldering period was shorter, approximately 3 h. The total duration of the fire was about 4 to 5 h, excluding the area that was burned later because of the helicopter's mechanical problems.

Figures 66.7 and 66.8 show estimates from the emissions-production model of heat release and the PM 2.5 production rate over time for the Creamery burn. Comparing these figures with figures 66.4 and 66.5 shows that the first nine subunits of the Creamery burned hotter and quicker than those in the Quinault burn.

Raymond Prescribed Burn

The Raymond prescribed burn occurred on 3 October 1994 and was ignited at about 1222 PDT. It was a 21.9-ha clearcut unit north of Raymond, Washington, on Weyerhaeuser timberlands (see figure 66.1). Woody fuels (primarily Douglas fir and hemlock) were again typical for the region, with a loading of about 45.6 Mg/ha. Forest-floor loading was 62.9 Mg/ha (3.8 cm deep). Fuel moisture content was about 28%. Total fuel consumption was estimated at 57.9 Mg/ha (table 66.1).

Table 66.1 Fuel moisture, loading, and consumption for the three prescribed burns

	Fuel diameter (cm)						Total woody fuel	Forest floor	Total woody plus forest floor
	0–0.5	0.5–2.5	2.5–7.5	7.5–23	23–50	50+			
Quinault									
Fuel moisture (%)		10		25					
Mass loading (Mg/ha)	5.8	9.6	16	49	110	68	260	120	380
Mass consumption (Mg/ha)	5.8	9.6	14	34	42	4.5	110	110	220
Percentage consumption	100	100	87	69	37	7	42	92	57
Creamery									
Fuel moisture (%)	—	12	—	28	—	—	—	—	—
Mass loading (Mg/ha)	3.6	6.1	16	20	11	5.6	63	42	100
Mass consumption (Mg/ha)	3.6	6.1	13	11	2.2	0	37	25	61
Percentage consumption	100	100	83	57	19	0	58	59	58
Raymond									
Fuel moisture (%)	—	12	—	28	—	—	—	—	—
Mass loading (Mg/ha)	3.6	5.2	11	20	4.5	1.6	46	63	110
Mass consumption (Mg/ha)	3.6	5.2	11	11	2.2	0	33	25	58
Percentage consumption	100	100	100	57	49	0	73	39	53

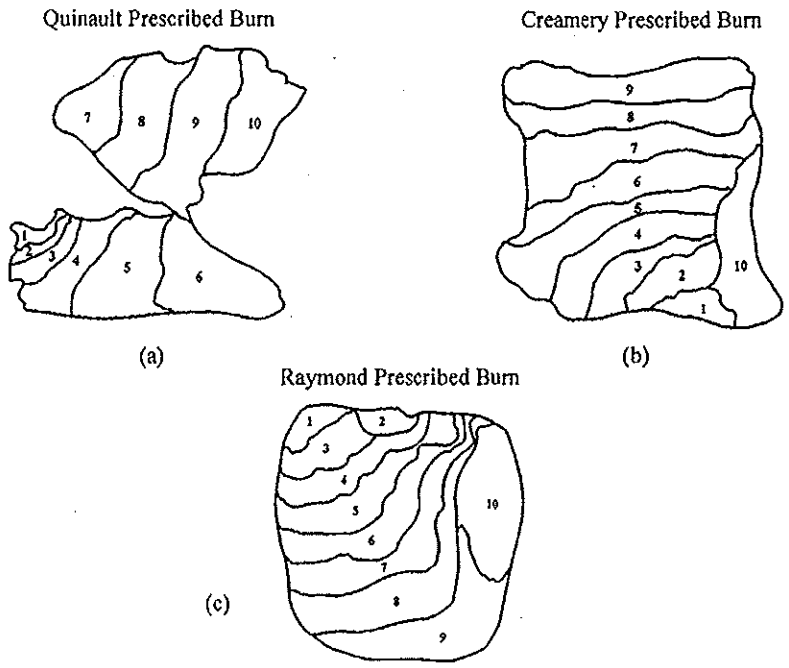

Figure 66.2 The ten subunits in each prescribed burn used to estimate fire progression and duration of combustion stage

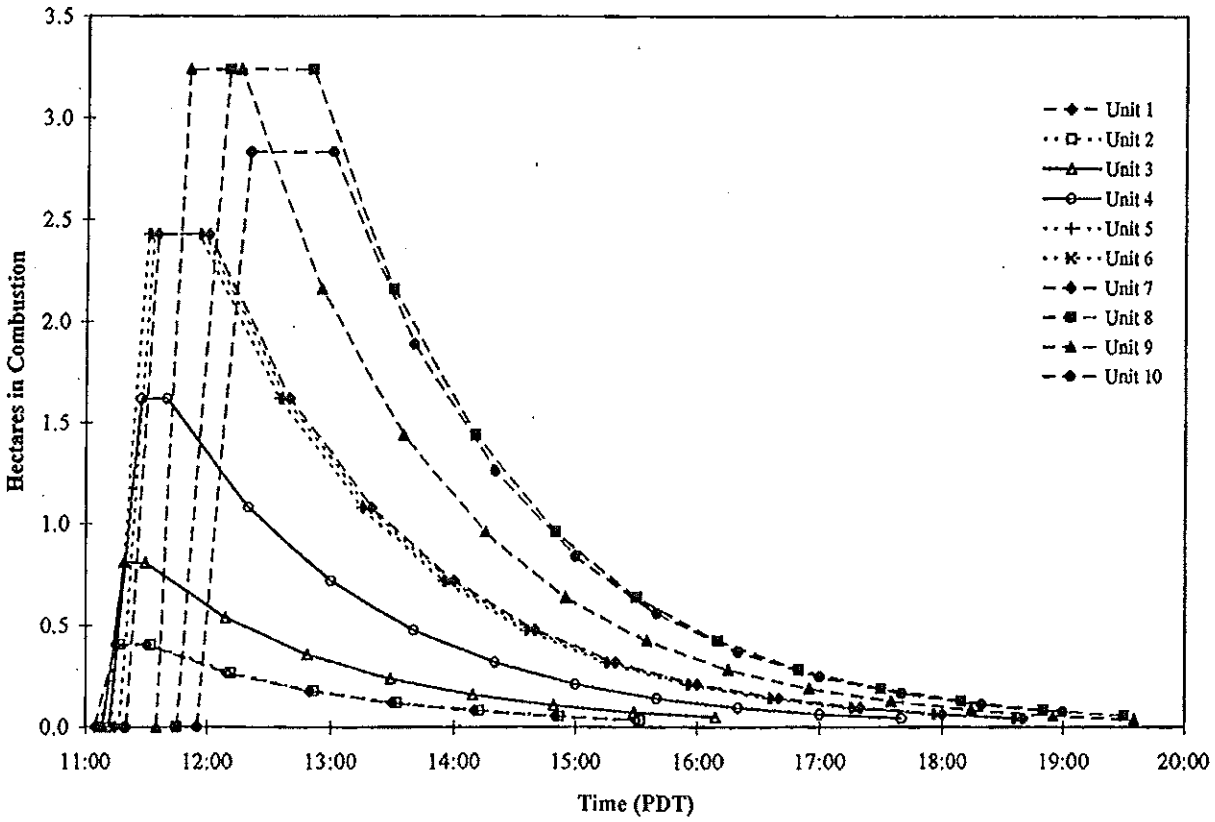

Figure 66.3 Combustion history for each subunit in the Quinault prescribed burn

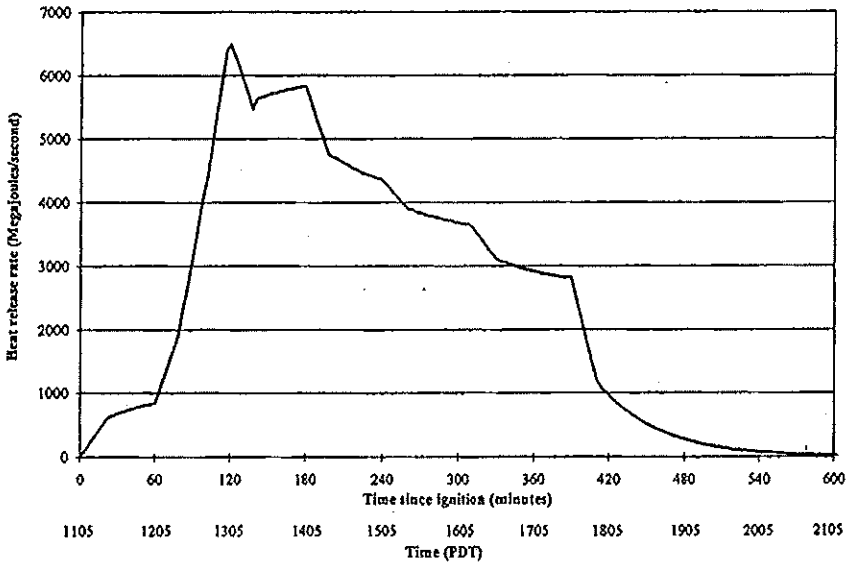

Figure 66.4 Heat released over time for the Quinault prescribed burn

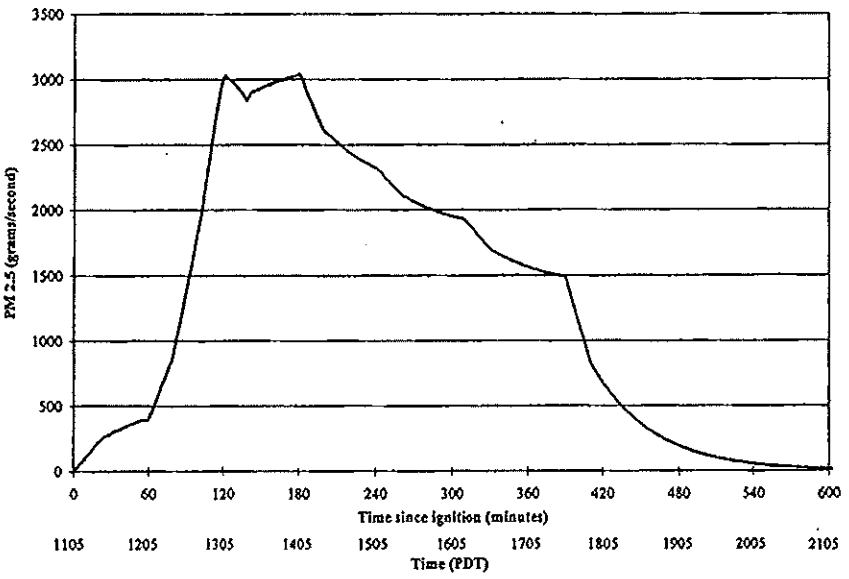

Figure 66.5 Estimates of PM 2.5 production over time for the Quinault prescribed burn

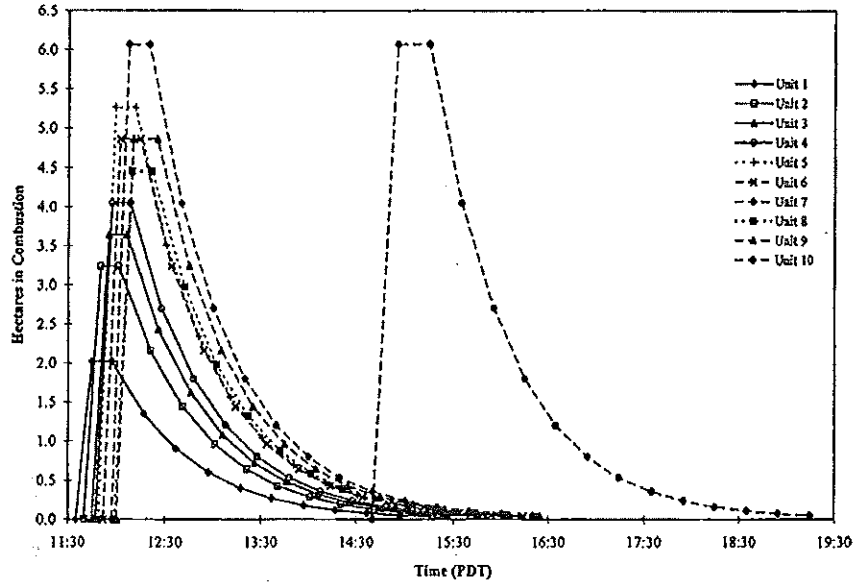

Figure 66.6 Combustion history for each subunit in the Creamery prescribed burn

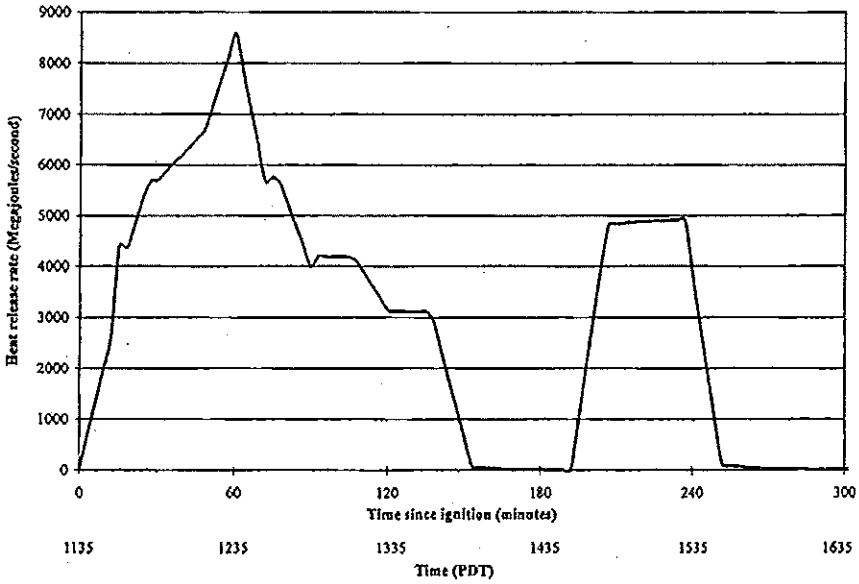

Figure 66.7 Heat release over time for the Creamery prescribed burn

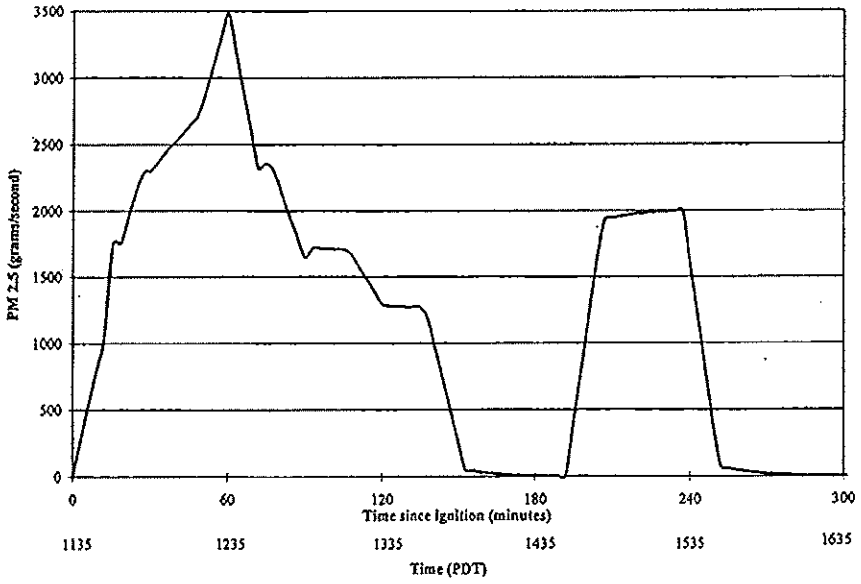

Figure 66.8 Estimates of PM 2.5 production over time for the Creamery prescribed burn

The subdivision of the site is shown in figure 66.2*c*, and the lighting pattern in figure 66.9. The Raymond prescribed burn took about 40 min. to ignite from a helicopter. Although the homogeneous small, woody fuel bed and steep slopes should have allowed quicker progression to maximum heat release and emissions production than observed at the Quinault burn, it did not. The higher fuel moisture content, higher humidities, and lower temperatures reduced the potential for a rapid buildup to flaming stage. Ground observations of plume and lighting indicated that the maximum heat-release rate probably occurred between 1250 and 1310 PDT. Because there was less large, woody debris and forest-floor material than on the Quinault site, and the woody fuel moisture content was slightly higher, the smoldering period was much shorter, approximately 2 h. The total duration of the fire was about 3 to 4 h. The heat release and PM 2.5 production rates from the emissions production model are shown in figures 66.10 and 66.11.

As in the Creamery burn (duration ca. 4 h), the Raymond burn (duration ca. 3.5 h) was shorter than the Quinault burn (duration ca. 10 h), and the higher fuel moisture content, smaller fuel loadings of large logs, and shallow duff resulted in a longer smoldering phase than for the Quinault burn.

Airborne Lidar Observations of the Smoke

The large fuel loading on the Quinault site allowed a substantial smoke plume to be generated with a smoldering period long enough to permit good measurements. The smoke in the vertical column above the burn, and in the plume that spread westward (over the Pacific Ocean) downwind of the burn, was sampled from the C-131A aircraft from about 1200 to 1500 h PDT.

A downward-pointing Nd-YAG lidar aboard the C-131A research aircraft was used to determine the spatial distribution of smoke mass in the plume from the Quinault burn, using the method described by Ross et al. (1996). Figure 66.12 shows a vertical lidar cross-section, obtained between about 1 h 49 min. and 1 h 54 min. after ignition, along the length of the smoke plume from the Quinault burn. It can be seen that the plume was about 400 m thick and increased in height by about 350 m as it drifted downward over a distance of about 25 km. The derived peak mass concentration of particles in the plume during this period is about 700 $\mu g\ m^{-3}$, located in a small region close to the fire. There is also a larger region, extending from about 8 to 14 km downwind, where the concentrations are 500 to 600 $\mu g\ m^{-3}$. Using the PDT times given in figures 66.5 and 66.12, comparisons can be made between the emission rates of PM 2.5 from the particle-mass production model and the particle mass concentrations at various distances downwind derived from the lidar measurements. For example, the results shown in figure 66.5 suggest rapid acceleration in smoke production starting about 60 min. after ignition. The lidar measurements, on the other hand, indicate that the rapid increase in smoke occurred somewhat earlier (around 40 min. after ignition).

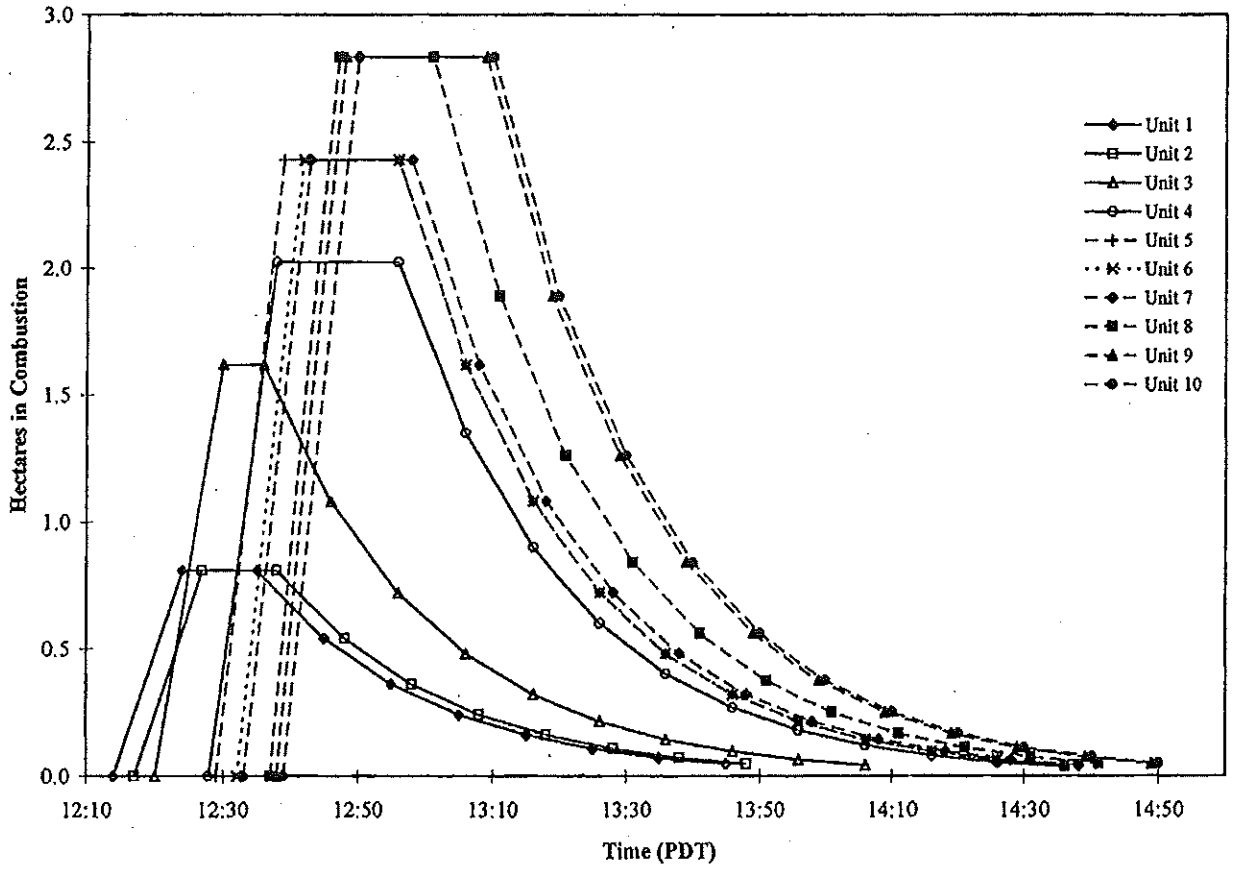

Figure 66.9 Combustion history for each subunit in the Raymond prescribed burn

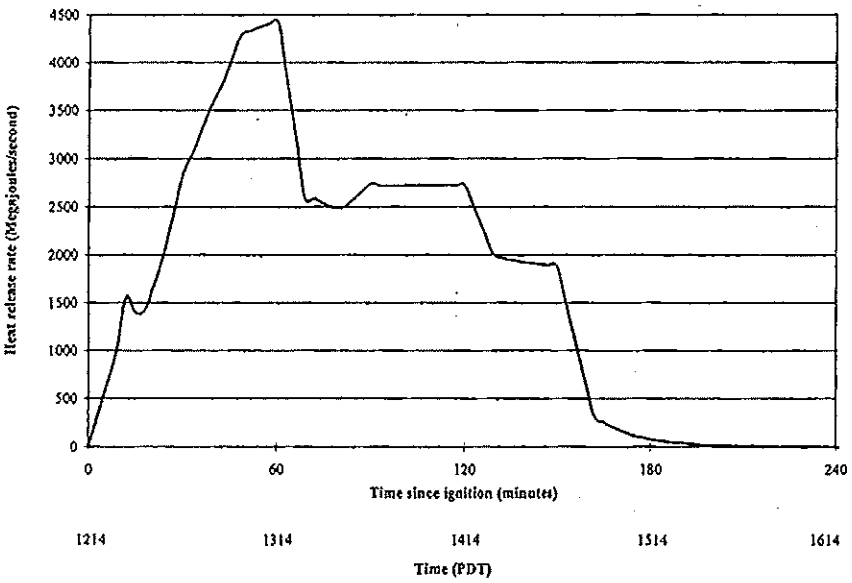

Figure 66.10 Heat-release rate over time for the Raymond prescribed burn

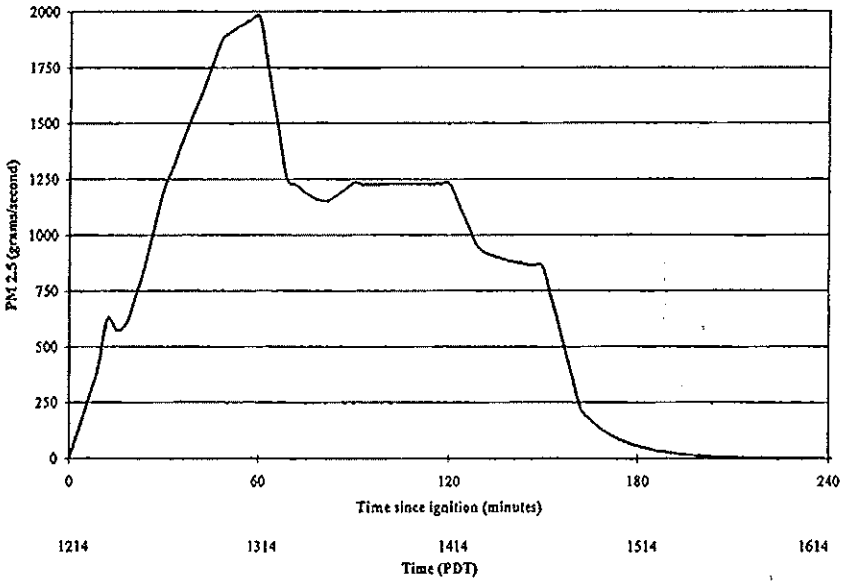

Figure 66.11 Estimates of PM 2.5 production over time for the Raymond prescribed burn

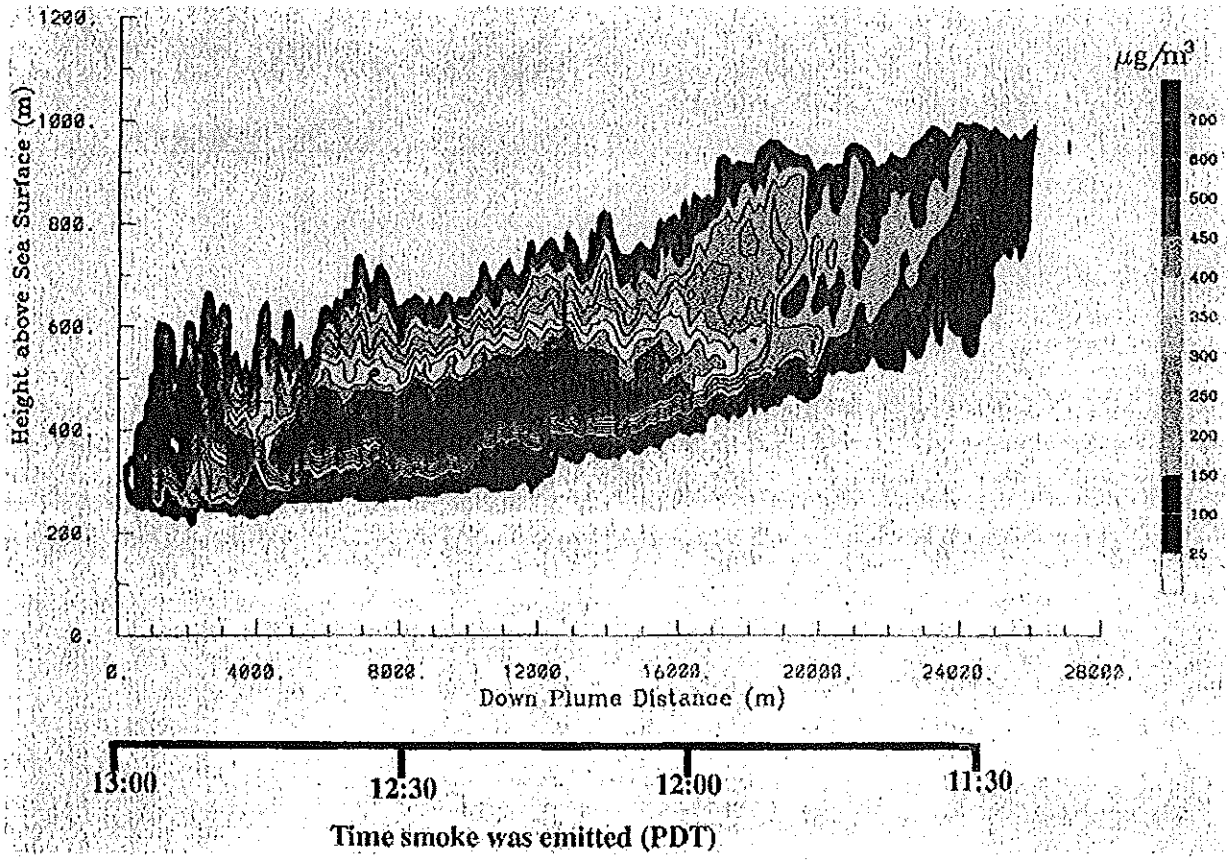

Figure 66.12 Vertical cross-section along the length of the smoke plume from the Quinault prescribed burn obtained with the airborne lidar between 1254 and 1259 PDT. The colors indicate the mass concentration of smoke particles in the plume derived from the lidar measurements.

Figure 66.13 shows two vertical sections across the width of the Quinault smoke plume obtained at about 1339 PDT and 3 km downwind and at 1402 PDT and 35 km downwind, respectively. The increase in the cross-sectional area of the plume with distance downwind is apparent; it can also be seen that the plume was still essentially coherent 35 km downwind. Since the mean wind speed in the boundary layer during the Quinault burn was about 4.5 m s^{-1}, the particles (or their precursors) for which concentrations are shown in figures 66.13*a* and *b* were emitted from the burn at about 1328 and 1152 PDT, respectively. From integration of the total mass concentrations of particles in the two vertical cross-sections shown in figure 66.13, and using the average wind speed through these sections, we can estimate the mass fluxes of particles emitted from the burn at 1152 and 1328 PDT, which are 3900 and 2100 g s^{-1}, respectively. These results are consistent with figure 66.3, which shows that at 1152 PDT, units 5, 6, and 7 were well into the flaming stage, unit 9 had reached its peak, and units 8 and 10 were beginning to burn. By contrast, figure 66.3 shows that by 1328 PDT the number of hectares in combustion was much lower. The mass flux derived from the lidar at 1152 PDT does not compare well with the emission-production model, which predicts a PM 2.5 flux of only 350 g s^{-1} at 1152 PDT (figure 66.5). However, at 1328 PDT the emission-production model predicts a PM 2.5 flux of about 2900 g s^{-1}, compared to 2100 g s^{-1}, derived from the lidar.

A recording of the burn, made on video from the aircraft, suggests that the smoke production accelerated faster than predicted by the emission-production model. For example, 1 h after ignition the video recording suggested that the smoke production was certainly more than one-seventh of the peak value shown in figure 66.5.

Evolution of Gases in the Smoke Plumes

Figure 66.14*a* shows measurements of the concentrations of NO, NO_x, SO_2, and O_3 along the long axis of the plume from the Quinault burn. The ratio of NO to NO_x was only one third just above the burn, indicating that much of the NO_x originated as nitrogen in the fuel (rather than through fixation of atmospheric nitrogen). Furthermore, because of the high rate of combustion, NO_x concentrations above the burn were high (~290 ppb). The measurements yield an emission factor for NO_x of about 1.1 g of nitrogen per kilogram of carbon burned. Assuming 70% NO_2 and 30% NO, this result is equivalent to 3.2 g of NO_x gases per kg of C burned.

The concentrations of ozone very close to the burn were below background values, which is to be expected due to the reaction of O_3 with the large amount of available particle surface area and NO in the smoke. However, in the presence of abundant NO_x and hydrocarbons, the concentration of O_3 increased rapidly downwind, reaching a peak value of about 80 ppb after just a half-hour travel time.

All three of the prescribed burns showed the same characteristic photochemistry: ozone production was rapid with concentrations above background within the first 15 min. of emission. Maximum ozone concentrations in these smoke plumes varied from 80 to 120 ppb at a mean plume age of 30 to 45 min.

The effects of plume dispersion on the concentrations of the gases can be removed by normalizing them to the excess (i.e., above ambient) CO_2 concentrations in the plume (shown in figure 66.14*b*), since CO_2 can be considered an approximate conservative tracer. The results are shown in figure 66.14*c*, which shows the CO_2-normalized concentrations of NO and NO_x generally diminishing with age, but the CO_2-normalized concentration of O_3 increasing with age. Thus, NO_x destruction in the smoke (presumably due to gas-to-particle conversion), as well as dispersion of the NO_x reduces the potential to produce ozone in the plume. Consequently, at a plume age in excess of about 30 min., the actual concentrations of O_3 in the plume diminish (see figure 66.14*a*).

Evolution of Particles in the Smoke Plumes

Effects of Phase of Burn on Particle Size Spectra

The life cycle of many prescribed burns of forest products can be divided into three phases: *ignition*, *flaming*, and *smoldering*. During the ignition phase, small pieces of biomass (<1 cm diameter), such as leaves and needles, are in full combustion, but larger pieces of biomass are still being heated radiatively to their combustion points. Large amounts of water vapor and volatile organics (from ether and benzene extractives) are outgassed during the ignition phase (Pyne 1984). For example, in the ignition phase of the Quinault burn, the relative humidity (RH) in the smoke plume very close to the burn was about 85%, but 30 min. later (in the flaming stage) it was 65% (ambient RH in the ambient air and in the boundary layer were 35% and 70%, respectively). Emissions during the ignition phase of a prescribed burn may,

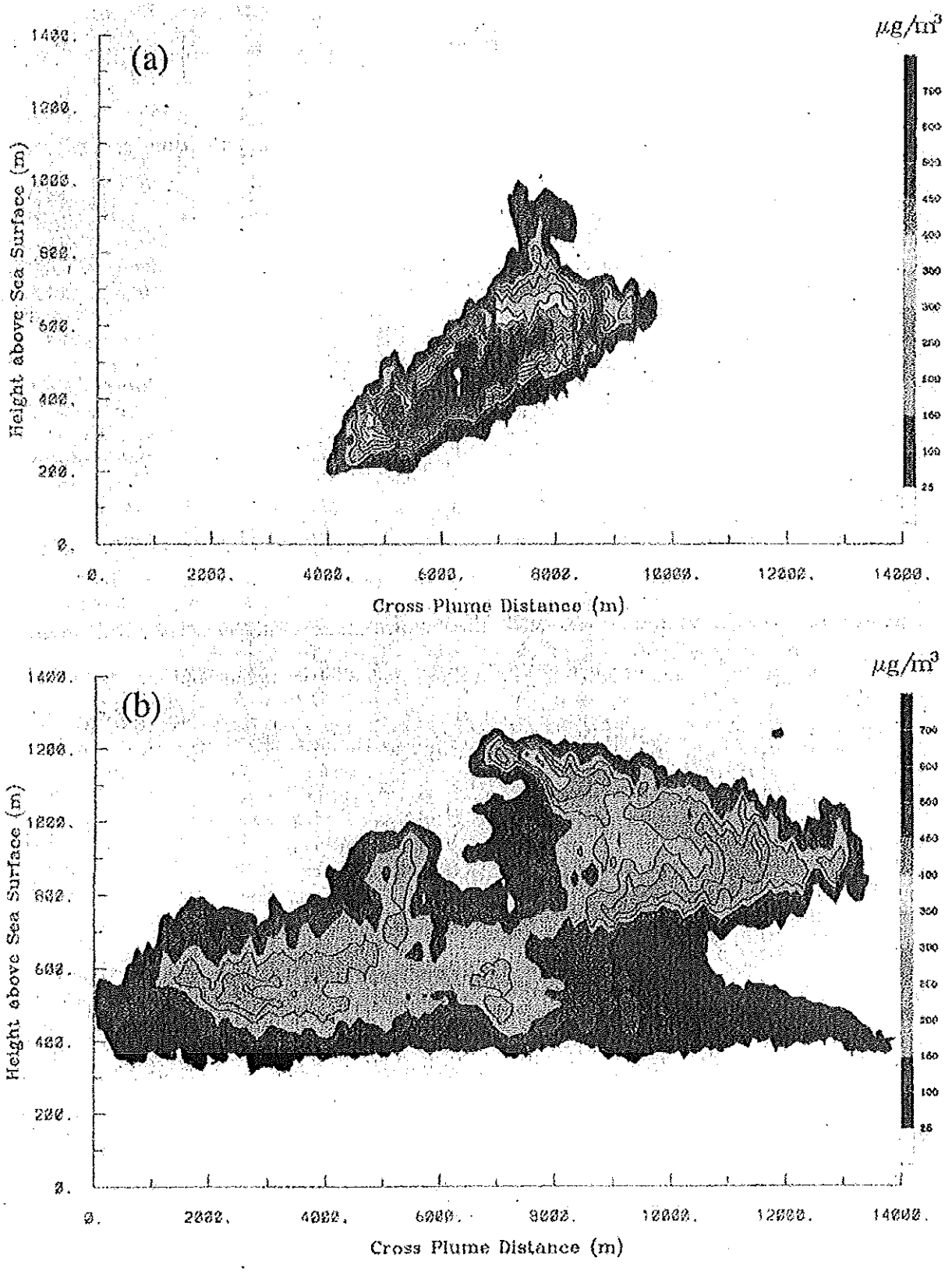

Figure 66.13 As for figure 66.12 but for vertical cross-sections across the width of the Quinault smoke plume obtained (*a*) at 1339 PDT and 3 km downwind of burn, and (*b*) at 1402 PDT and 35 km downwind of the burn

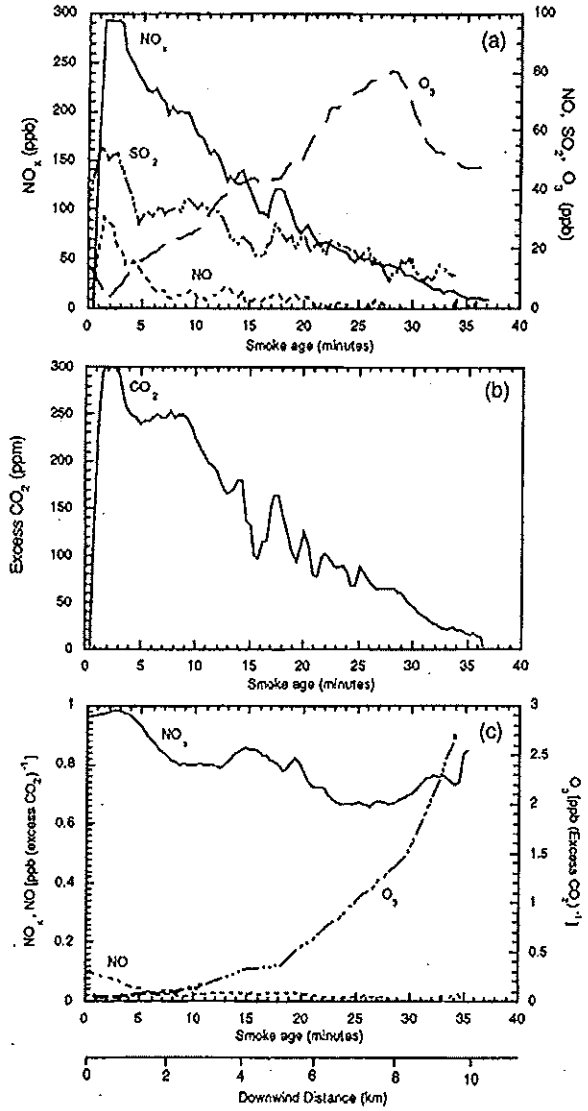

Figure 66.14 Measurements along the long axis of the smoke plume from the Quinault burn of (*a*) NO, NO_x, O_3, and SO_2 concentrations; (*b*) excess CO_2 concentrations; and (*c*) CO_2-normalized NO, NO_x and O_3 concentrations

under some circumstances, be determined by the fuel used to ignite the burn (e.g., helitorch, gasoline) as well as by the biomass itself. The length of the ignition phase is highly variable, since it depends on the water content, density, and size of the biomass. Prescribed burns often have quite a short ignition phase, because ignition generally occurs when the small fuels are dry. For example, for the three prescribed burns discussed here the ignition phases were less than 15 min.

The flaming phase starts when the larger pieces of biomass reach a temperature at which exothermic reactions can take place, which is about 325°C for pilot flame and 600°C for spontaneous combustion (Chandler et al. 1983). By this time, a char layer has formed on the surfaces of the larger pieces of fuel and so they can support steady flames.

Fuel components in the flaming phase can be broken down into: cellulose (50–65%), lignins (16–35%), extractives (0.2–15%), minerals, and water (Pyne 1984). Although the set of the several hundred elementary reactions governing combustion is not completely understood, the general reaction can be approximated by the combustion of cellulosic fuels (Pyne 1984):

$$C_6H_{12}O_6 + 6\,O_2 \rightarrow 6\,CO_2 + 6\,H_2O + 1.26 \times 10^6\,kJ$$

The smoldering phase occurs when the volatiles have been expelled from the cellulose fuel, leaving a charcoal shell (Chandler et al. 1983). At this point, oxygen reacts with carbon directly at about 600°C and heat production is only a third that of complete combustion. If temperatures are increased to 650 to 700°C, CO can convert to CO_2. Thus, temperatures are reduced compared to the flaming phase.

The different phases in combustion have significant effects on particle emissions. Shown in figure 66.15 are emission factors (i.e., number and volume of particles emitted per unit mass of carbon burned) versus particle diameter for the three phases of combustion of the Raymond burn. In the ignition phase the emission factors are relatively low over all particle sizes. Also, the various modes in the particle size distribution for the ignition phase indicate that several processes are at work. The particle number and volume emission factors for the flaming phase are greater than those in the ignition phase for particles >0.03 μm diameter, and for particles of ~ 0.3 μm diameter (which dominate the optical properties of the smoke) they are nearly three orders of magnitude greater. Also, as combustion shifts from the ignition to the flaming phase, the particle mode shifts to a larger size (figure 66.15). It does so because vigorously flaming fires produce high con-

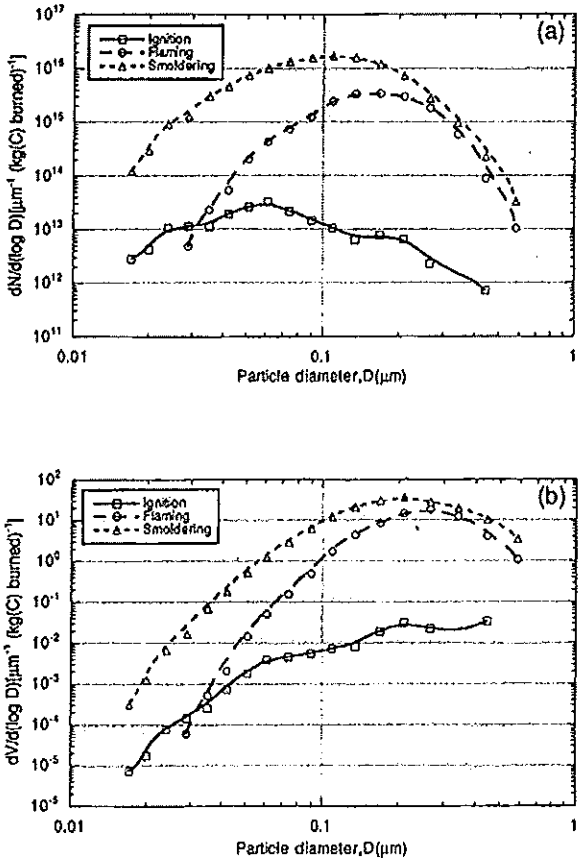

Figure 66.15 Emission factors versus particle diameter for (*a*) number distributions, and (*b*) volume distributions of smoke particles for the ignition, flaming, and smoldering phases in the Raymond prescribed burn

centrations of small particles that coagulate rapidly in the plume to produce larger particles.

During the smoldering phase in combustion the particle number and volume emission factors increase still further above that for the flaming phase (figure 66.15). However, the fire temperatures and particle concentrations are much lower; consequently, particle coagulation and the particle mode size is reduced (figure 66.15).

Figure 66.16 shows how the particle size distribution evolved during the ignition and flaming stages in combustion of the Creamery burn. In these plots the particle concentrations have been normalized by dividing them by the excess concentration of CO_2 in the plume. Thus, the effects of plume dispersion are essentially removed in figure 66.16. The size spectrum shown for "early ignition" in figure 66.16 was measured 15 min. after the fuel was ignited; at this time

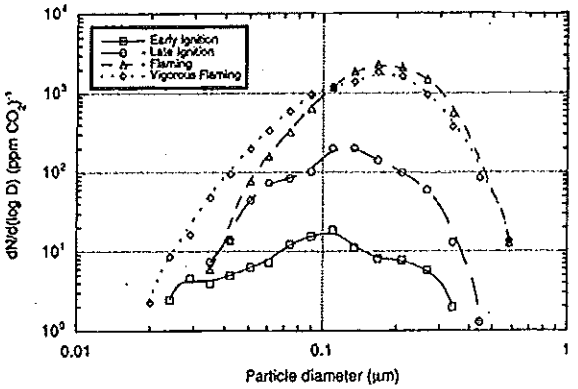

Figure 66.16 Evolution of the smoke-particle number concentrations (normalized to the excess concentration of CO_2) during the early phases in the Creamery prescribed burn

emissions from the ignition fuel probably were present in the smoke. The spectrum labeled "late ignition" was measured 25 min. after ignition, by which time any effects of the ignition fuel should have been overwhelmed by the smoke from the biomass fuel. The increasing concentrations of particles produced an increase in particle mode radius. Fifteen minutes later (i.e., 40 min. after ignition) the flaming stage was reached. Now the temperature of the burn, and the concentration of particles produced, are at their highest and the particle mode size reaches a maximum value of ~ 0.2 μm (figure 66.16). Later on the same day, a small (6 ha) unburned portion of the site was reignited and the spectrum labeled "vigorous flaming" in figure 66.16 was obtained. The particle size distribution is similar to that labeled "flaming" but somewhat broader (possibly because the burn area was smaller, which allowed the fire to burn more efficiently and to produce small particles).

Effects of Time on Evolution of Particles in Smoke Plumes

Figure 66.17 shows the time evolution of the CO_2-normalized particle number and volume distributions for the early flaming phase in combustion of the Quinault burn. The particle size spectra were measured at the top of the smoke column above the burn (labeled "source") and after a smoke parcel had aged for about 1.8 h. Over this period the peak concentrations were decreased dramatically by coagulation, and the particle-number mode shifted from 0.16 to 0.28 μm and the particle volume mode from 0.25 to 0.38 μm.

As we have seen, there was rapid ozone production in the plume from the Quinault burn, which indicates

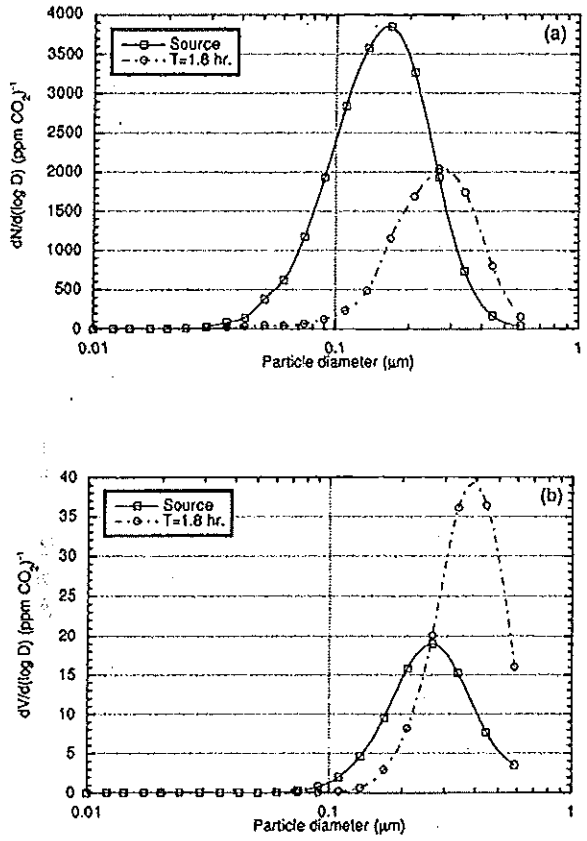

Figure 66.17 Particle-size distribution in the smoke from the early flaming phase in the Quinault prescribed burn at source and 1.8 h downwind. (*a*) Number distribution, and (*b*) volume distribution. Particle concentrations are normalized to excess CO_2 concentrations.

high photochemical activity. Therefore, significant gas-to-particle (g-to-p) conversion is to be expected. Indeed, over the 1.8-h interval that separates the two spectra shown in figure 66.17, the ratio of SO_2-to-excess CO_2 decreased by about 60%. In view of the very high particle concentrations in the plume, the overwhelming majority of the condensed gases must have been deposited onto existing particles rather than forming new particles. Therefore, some of the increase in particle mode size shown in figure 66.17 was probably produced by g-to-p conversion.

The total particle volume in figure 66.17*b* increases by a factor of two in the 1.8-h period. This growth can be attributed to absorption of water vapor and/or g-to-p conversion. For the Quinault burn, the average RH of the ambient air at the height of the plume was 35%. At the location in the plume where the spectrum labeled "source" was measured, the RH was 80%. It is likely that as the RH approached 80% some of the smoke particles deliquesced, which would increase their mass by a factor of about 1.5 (Hanel 1976).

We can get a rough idea about the importance of deliquescence in increasing the mass of the smoke particles as follows. First we can compare the mass concentrations of particles derived from differential mobility particle sizing (DMPS) measurements (at the RH of the plume) with those derived from filters exposed to the smoke, which were weighted at an RH of 15%. Assuming an average smoke particle density of 1.5 g cm^{-3}, the mass concentrations of smoke at the "source" derived from the DMPS and filter measurements were 2200 and 1800 $\mu g\ m^{-3}$, respectively; this reading implies that about 18% of the mass of the smoke particles at the "source" was water. For the spectrum measured at 1.8 h, the corresponding derived particle concentrations were 700 and 360 $\mu g\ m^{-3}$, respectively. Thus, about 51% of the total mass at 1.8 h can be ascribed to condensed water and high-volatility organics. Since the CO_2-normalized particle volume increased by a factor of 2 over the same 1.8-h period (figure 66.17*b*), the increase in particle volume attributed to water is $(0.51)(2) - (0.18)(1) = 0.84$ or 84%. The remaining mass increase of 16% could have been due to heterogeneous nucleation of sulfates and nitrates. It is interesting to compare these results with those of Kaufman et al. (1994) and Fraser et al. (1984), which are based on Hanel (1981), who assumed that at 70% RH, liquid water comprises 50% of the mass of smoke particles.

Asymmetry of Smoke Particles

A measure of the asymmetry (i.e., deviation from sphericity) of the smoke particles was obtained using the aerosol asymmetry analyzer described by Weiss et al. (1992). Since the light-scattering coefficient of the smoke particles from the Quinault burn changed by <2% as an applied electric field was reversed in direction (figure 66.18*a*), the particles must have been essentially spherical. This configuration contrasts with the smoke produced by the 1991 Kuwait oil fires, for which the light-scattering coefficient changed by about 30% as the electric field was reversed (figure 66.18*b*, and Weiss et al. 1992).

Cloud Condensation Nucleus Spectra

Cloud condensation nucleus (CCN) spectra were measured aboard the Convair C-131A aircraft with the four-channel vertical-plate, continuous-flow, thermal diffusion chamber described by Radke et al. (1981).

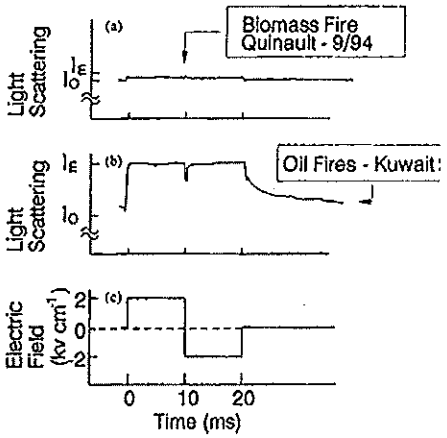

Figure 66.18 Comparison of changes in the light-scattering coefficient of smoke particles with change in direction of an electric field in (*a*) smoke from the Quinault prescribed burn, and (*b*) smoke from the 1991 Kuwait oil fires. The applied electric field is shown in (*c*).

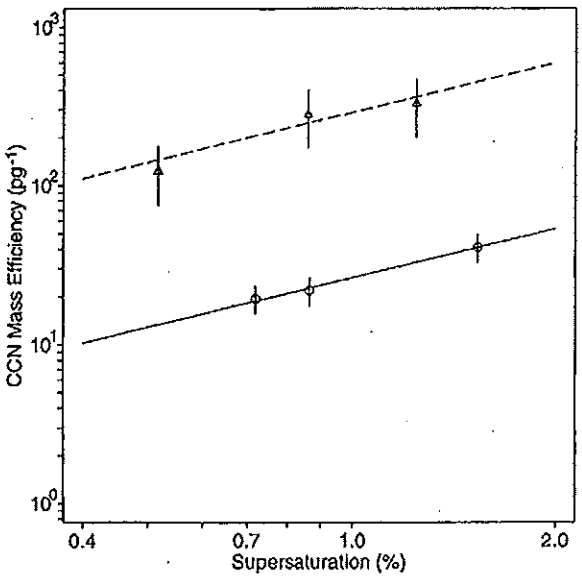

Figure 66.19 Cloud condensation nucleus (CCN) concentrations per particle mass concentration versus supersaturation of air measured in the smoke from the Quinault burn at 0.2 h (circles and solid line) and 1.8 h (triangles and dashed line) smoke travel time from the burn

CCN concentrations in the smoke were as much as 1000 times greater than in the background air and, despite dispersion of the plume, they increased with downwind distance as the smoke aged. The effects of dispersion on the concentration of CCN can be removed by dividing the measured CCN concentrations at any point in the plume by the mass concentration of smoke at that point, to give the *CCN mass efficiency* (units: number of CCN per picogram of smoke, or pg^{-1}). Figure 66.19 shows plots of CCN mass efficiencies measured in the smoke close to the Quinault burn (~0.2-h travel time downwind) and 25 km from the fire (~1.8-h travel time). As can be seen, the CCN mass efficiencies of the smoke are about a factor of ten greater at 1.8-h travel time than at 0.2 h. We attribute this increase to the progressive accumulation of water-soluble ionic and organic species onto the smoke particles as they age.

The CCN mass efficiency at 1% supersaturation for the more aged smoke sample shown in figure 66.19 is ~300 pg^{-1} or 3×10^{14}/g of smoke. The corresponding PM 3.5 emission factor for the Quinault burn was ~50 g/kg of C burned (see table 66.2). Assuming a C mass fraction of 50% for the fuel (Bryam 1959), this result translates to a value of 5 g/kg of fuel. Thus, a CCN mass efficiency of 3×10^{14} g^{-1} suggests the production of ~7.5×10^{12} CCN (at 1% supersaturation)/g of fuel burned. For comparison, Warner and Twomey (1967) burned sugarcane leaf in the laboratory and found ~5×10^{12} CCN (at 1% supersaturation)/g of fuel, and Dinh et al. (1992), who obtained a value of 10^{11} CCN (at 0.1% supersaturation)/g of fuel for savanna grass burning.

The straight-line fits to the data points in figure 66.19 can be represented by:

$$(CCN)_{me} = c(SS)^k$$

where $(CCN)_{me}$ is the CCN mass efficiency (in pg^{-1}), SS the supersaturation in %, and c and k are empirical constants. The values of c and k for the data shown in figure 66.19 are $c = 25 \pm 5$ pg^{-1} and $k = 1.0 \pm 0.1$ for the 0.2-h-old smoke, and $c = 290 \pm 120$ pg^{-1} and $k = 1.0 \pm 0.1$ for the 1.8-h-old smoke.

Optical Properties of the Smoke

Light-Scattering Coefficients and the Mass Scattering Efficiency

Measurements of the light-scattering coefficient, σ_s, at a wavelength of 540 nm, reached a maximum value of about 17 km^{-1} in the dense smoke directly above the prescribed burns and decreased downwind as the smoke plume dispersed. A plot of σ_s for a typical penetration along the long axis of the smoke plume from the Quinault fire is shown by the solid line in figure 66.20.

Table 66.2 Some emission factors for the Quinault, Creamery, and Raymond prescribed burns during their flaming stages of combustion and for the Corral wildfire during smoldering combustion

Burn	CO_2[a]	CO[a]	NMHC[a]	CO_4[a]	NO[b]	NO_x[c]	SO_2[d]	Organic carbon[a]	Black carbon[a]	PM 3.5[e]
Quinault	789.6	139	25.9	21	0.85	3.8	2.59	23.2	1.26	51
Creamery	837	88	24	19	1.82	6.7	4.5	29	2.43	54
Raymond	838	118	20	10	0.65	3.4	1	12.7	0.98	65
Corral (wildfire)	715	168	66.52	27	0.56	1.29	0.79	21.31	1.73	82.7

a. g C/kg C burned.
b. g NO/kg C burned.
c. g N/kg C burned.
d. g SO_2/kg C burned.
e. g particulate matter with diameter approximately <3.5 μm/kg C burned. The particle range is approximate, due to penetration losses associated with the aircraft inlet. The size cut was determined experimentally.

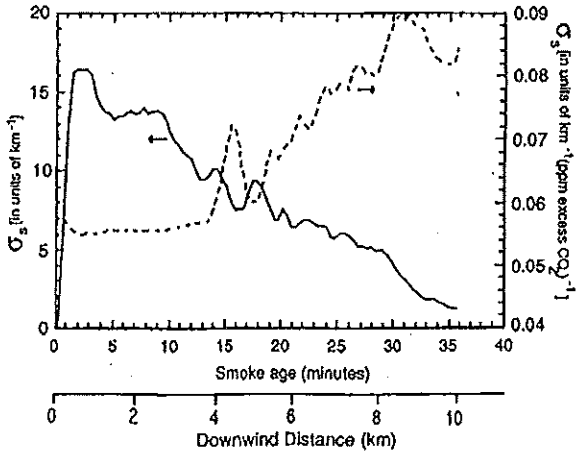

Figure 66.20 Light-scattering coefficient (σ_s, solid line) and CO_2-normalized light-scattering coefficient (dashed line) measured along the long axis of the smoke plume from the Quinault burn

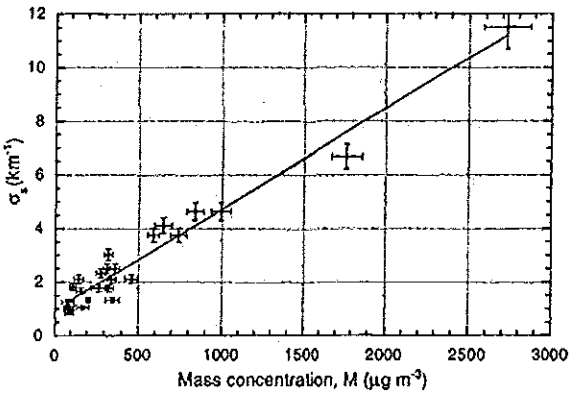

Figure 66.21 Light-scattering coefficient vs. mass concentration of particles using data from all three prescribed burns. The line represents the least-squares best fit to the data. The slope of the line is the average value of the (dry) mass scattering efficiency of the smoke.

Assuming the dispersion rate for fine particles is similar to that of CO_2, we can normalize the excess σ_s values to excess CO_2 to account for plume dispersion (dashed line in figure 66.20). From this normalization we see that σ_s/CO_2 increased by a factor of 1.6 over a 30-min. period. This expansion is the result of the steep increase in particle-scattering efficiency (Q_{scat} for particles in the 0.1 to 0.5-μm size range. Since the smoke was heated in a plenum chamber prior to sampling by the nephelometer, the increase in the σ_s/CO_2 ratio cannot have been due to water vapor or high-volatility organics. Instead it indicates that a high rate of particle coagulation and/or heterogeneous nucleation was occurring.

Figure 66.21 shows a plot of σ_s versus simultaneous measurements of the mass concentration (M) of smoke (from weighed Teflon filters) using data from all three of the prescribed burns. The line shown in figure 66.21, which is the least-squares best fit to the data, is represented by:

$$\sigma_s = 3.8 \times 10^{-3}\mathrm{M} + 0.95 (r^2 = 0.95)$$

where σ_s is in km^{-1} and M in μg m^{-3}. Hence, the (dry) mass scattering efficiency of the smoke is 3.8×10^{-3} km^{-1} (μg m^{-3})$^{-1}$ or 3.8 m^2 g^{-1}.

An increase in the mass scattering efficiency might be expected with increasing distance downwind of a burn due to particle coagulation and heterogeneous chemistry (see figure 66.17, which shows a threefold increase in the number of particles between 0.3 and 0.5 μm diameter at 1.8 h downwind for the Quinault burn). In an effort to gauge these effects, Mie calculations (at $\lambda = 540$ nm and assuming a real part of the refractive index of 1.5) were performed on the particle size spectra shown in figure 66.17. The results are shown in figure 66.22, which is a plot of $d\sigma_s/d$ (log D) normalized to excess CO_2 versus particle size. There-

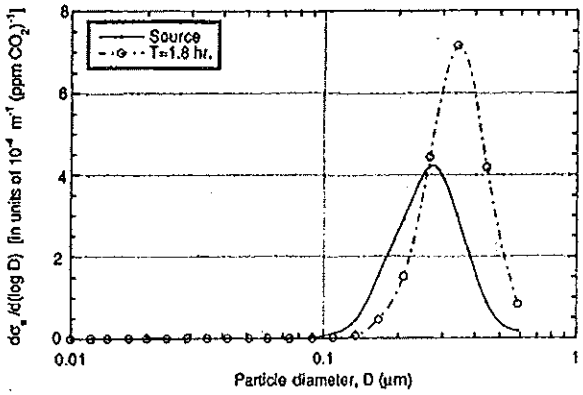

Figure 66.22 CO_2-normalized values of $d\sigma_s/d(\log D)$ versus $\log D$ for the particle spectra shown in figure 66.17

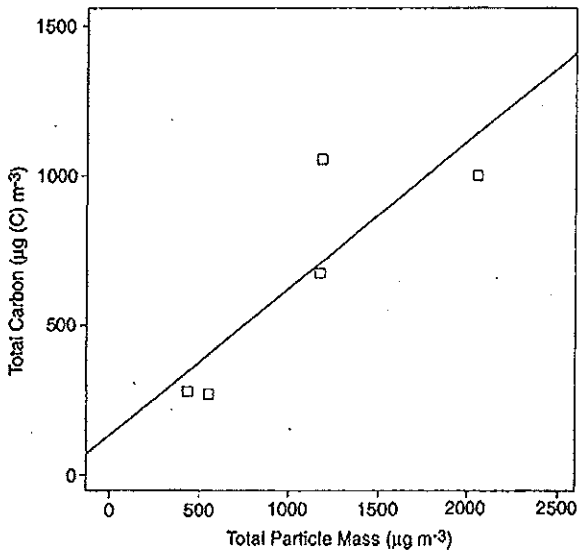

Figure 66.23 Total particulate carbon versus total particulate mass. The line represents the least-squares fit through the data points. The slope of the line (i.e., 0.49) is the mean C content of the smoke particles.

fore, the areas under the curves in figure 66.22 are CO_2-normalized light-scattering coefficients. It can be seen from figure 66.22 that the growth of the smoke particles over 1.8 h produced a doubling in the CO_2-normalized light-scattering coefficients, despite the reduction in the overall number of particles. The CO_2-normalized values of σ_s shown in figure 66.20 give another indication of this effect. However, because of the changing combustion efficiency (i.e., the percentage of fuel carbon emitted as CO_2) during this stage of the Quinault burn, it is not clear how much of the observed variations in the CO_2-normalized scattering coefficient were due to changes in burning conditions or to changes in the size distribution of the smoke particles.

Light-Absorption Coefficients and Single-Scattering Albedo

The ability of smoke particles to absorb light is mainly determined by the amount of black carbon (or soot) in the smoke particles. This quantity, in turn, strongly depends on the phase of combustion, because smoke from the flaming phase contains considerably more black carbon than smoke from the smoldering phase (Patterson and McMahon 1984).

Our measurements of the ratio of black carbon to total C (i.e., black + organic) in the smoke from the Quinault and Creamery burns ranged from 5 to 8%. By comparison, Mazurek et al. (1991) reported ratios ranging from 1 to 10% for a prescribed burn in Ontario. The lowest ratio of black to total C that we measured was from the only pure smoldering sample collected; all the other samples were of mixed-phase smoke. Cachier et al. (1991) found that for smoke from savanna fires the relative concentrations of black carbon are higher for flaming combustion than for smoldering. On average, in our measurements total C accounted for ~50% of the total mass of aerosol sampled in the smoke plumes (figure 66.23).

A summary of our measurements of the related optical properties of the smoke from the three prescribed burns, and from the Corral wildfire, is shown in table 66.3. Parallel measurements of σ_s and the total light-extinction coefficient (σ_e) at a wavelength of 540 nm permitted derivation of the light-absorption coefficient ($\sigma_a = \sigma_e - \sigma_s$) and the single-scattering albedo ($\omega = \sigma_s/\sigma_e$). Several examples of σ_s and σ_e measurements across transects of the smoke plumes from the three prescribed burns are shown in figure 66.24; in these plots the shaded region between the two curves represents optical absorption.

The measurements of the single-scattering albedo of the smoke (table 66.3) range from 0.74 (for ignition-phase smoke) to 0.98 (for smoldering-phase smoke). Both extremes were measured in the smoke from the Creamery burn, which displayed a very clear progression in the optical properties of the smoke. The Creamery burn was the only one during which we sampled smoke from early in the ignition phase to well after the commencement of pure smoldering. In the Quinault burn, we obtained no samples of smoke that were entirely representative of a particular phase of

Table 66.3 Summary of measurements of optical property for the smoke from three prescribed burns and from the Corral wildfire

Burn	Time smoke was sampled from aircraft (PDT)	Age of smoke sample[a] (min.)	Time of emission of smoke sample (PDT)	Combustion phase(s) at time of sample emission[b]	σ_s^c (in units of 10^{-3} m^{-1})	σ_a (in units of 10^{-3} m^{-1})	ω^d
Quinault	1146	5–20	1125–1145	I, F, S	10.1	1.9	0.84
	1155	5–25	1130–1155	I, F, S	11.1	1.8	0.86
	1200	10–25	1135–1200	I, F, S	10.5	1.2	0.90
	1242	30	1210	I, F, S	8.6	1.2	0.88
	1309	40–70	1200–1230	I, F, S	8.1	0.7	0.92
	1357	100–120	1200–1220	I, F, S	3.6	0.5	0.88
Creamery	1144	10	1135	I	2.9	1.1	0.74
	1150	5	1145	I, F	6.6	1.5	0.82
	1201	15	1145	I, F	5.7	0.9	0.87
	1212	10	1200	I, F, S	8.3	0.9	0.90
	1218	20	1155	I, F, S	2.9	0.3	0.92
	1224	20	1205	I, F, S	6.8	0.3	0.96
	1247	30–45	1205–1220	F, S	9.1	0.3	0.97
	1406	40	1325	S	8.7	0.2	0.98
	1436	80	1310	S	3.6	0.1	0.97
Raymond	1258	10	1250	F, S	4.2	0.3	0.94
	1313	5	1305	F, S	5.4	0.3	0.95
	1317	<5	1315	S	7.1	0.6	0.92
	1348	20	1325	S	2.6	0.1	0.97
	1427	<5	1425	S	5.5	0.2	0.96
Corral Wildfire	1548–1701	—	—	—	3.2–6.9	0.2–0.9	0.89–0.95

a. Age is based on the mean distance from the burn during sampling and mean boundary-layer wind speeds of 5 m s^{-1} for the Quinault and Creamery burns, and 10 m s^{-1} for the Raymond burn. A single value for the age of the sample indicates the aircraft flew across the plume axis perpendicular to the mean wind vector. A range of ages indicates the aircraft flew along the plume axis parallel to the mean wind vector. The error in estimates of age is about ±30%; this uncertainty propagates to the estimates on the time of emission of the smoke samples.
b. I ignition; F flaming; S smoldering.
c. Peak values measured in plume transect.
d. Average across plume transect.

combustion. Instead, all our smoke samples from this burn contained a mixture of smoke from the three phases in combustion. Consequently, our measurements of the single-scattering albedo of the smoke from this burn vary over a narrower range (0.84–0.92). In the Raymond burn, all samples contained some smoldering smoke, but we did take measurements in at least two samples of pure smoldering smoke. A third sample (at sample time 1317 PDT) is categorized as smoldering, although this designation is uncertain because of the unusually low value of the single-scattering albedo. Our measurements of the single-scattering albedo in the smoke from the Raymond burn range from 0.92 to 0.97. The samples listed in table 66.2 can be associated with the approximate stage in the life cycle of any of the three prescribed burns by comparing the estimated emission times in table 66.3 with figures 66.3, 66.6, and 66.9. A range of values is listed for the Corral wildfire, for we have very little information on the burning conditions in this fire.

We can use the mass scattering efficiency to indirectly estimate the absorption efficiency (also called the specific absorption) of the smoke from the data shown in table 66.2. Assuming a mass scattering efficiency of 4 m^2 g^{-1} (figure 66.21), the two extreme values for the single-scattering albedo in table 66.2 suggest a range of values of 0.1 to 1.5 m^2 g^{-1} for the specific absorption of the various smokes.

Emission Factors

Emission factors (i.e., mass of a material emitted per unit mass of fuel burned) were derived by the carbon-balance technique (Radke et al. 1988). The results are shown in table 66.2 for the three prescribed burns as well as for a wildfire (the Corral fire in Idaho, 27 September 1994).

In the three prescribed burns, the emission factors measured during the flaming period in combustion were fairly similar. However, for the Creamery burn, the emission factors for NO_x and NO are greater than those for the other two burns. This difference may have come about because the Creamery burn supported the highest combustion/unit area of the three burns.

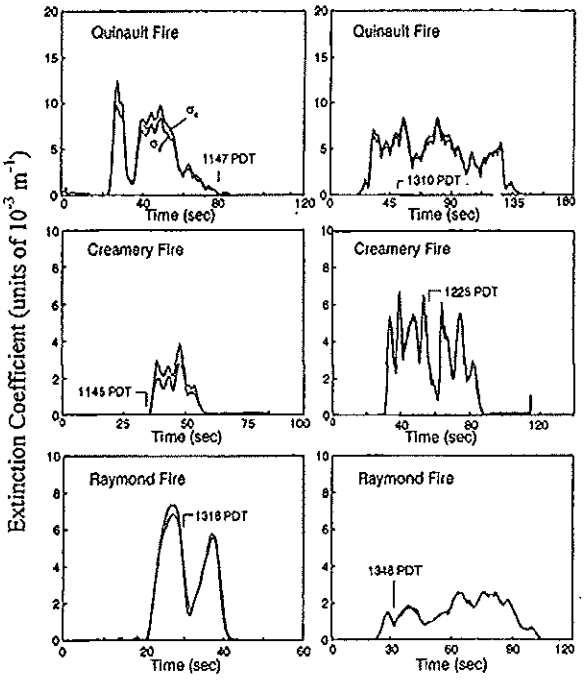

Figure 66.24 Selected optical extinction measurements at a wavelength of 540 nm in the smoke plumes from the three prescribed burns. In each plot the upper curve is total light extinction and the lower curve the light extinction due to scattering. The shaded area between the two curves represents extinction due to absorption.

Furthermore, the Creamery burn had the highest combustion efficiency (90%).

It is interesting to compare the emission factors for the three prescribed burns to that of the Corral wildfire in the smoldering-combustion phase. The combustion efficiency in the Corral wildfire was 81%, and so a moderate amount of combustion was still occurring. The emission factors for the Corral wildfire for nonmethane hydrocarbons, methane, and particulate matter were significantly higher than those for the three prescribed burns, but the emission factor for NO_x was significantly lower due to the lower combustion temperature.

Acknowledgments

Thanks are due to the flight crew of the Convair C-131A, and to Ronald Ferek for useful discussions. We also thank the Washington State Department of Natural Resources, Oregon State Department of Forestry, the Quinault Tribe, Tillamook Creamery Company, and Weyerhaeuser Timber Company, for allowing us to monitor the prescribed burns. This research was supported by NASA grants NAGW-13750 and NAG1-1709 and by EPA grant CR822077. These agencies have not officially reviewed this article; therefore, their endorsement should not be inferred.

References

Bryam, G. M. 1959. Combustion of forest fuels. In *Forest Fire Control and Use*, edited by K. P. Davis, New York, McGraw-Hill.

Cachier, H., J. Ducret, M. P. Brémond, V. Yoboué, J. P. Lacaux, A. Gaudichet, and J. Baudet. 1991. Biomass burning aerosols in a savanna region of the Ivory Coast. In *Biomass Burning: Atmospheric, Climatic and Biospheric Implications*, edited by J. S. Levine, Cambridge, Mass., MIT Press, pp. 174–180.

Chandler, C., P. Cheney, P. Thomas, L. Trabaud, and D. Williams. 1983. Fire in forestry. In *Forest Fire Behavior and Effects*, vol. 1. New York, John Wiley, 1–30.

Dinh, P. V., J. P. Lacaux, and R. Serpolay. 1992. Cloud forming properties of biomass burning aerosols. In *Nucleation and Atmospheric Aerosols*, edited by N. Fukuta and P. E. Wagner, A. Deepak Publishing, pp. 173–176.

Fraser, R. S., Y. J. Kaufman, and R. L. Maloneh. 1984. Satellite measurements of aerosol mass and transport. *Atmos. Environ.*, 18, 2577–2584.

Hanel, G. 1976. The properties of atmospheric aerosol particles as functions of relative humidity at thermodynamic equilibrium with the surrounding moist air. *Adv. Geophys.*, 19, 73–188.

Hanel, G. 1981. An attempt to interpret the humidity dependencies of aerosol extinction and scattering coefficients. *Atmos. Environ.*, 15, 403–406.

Kaufman, Y. J., B. N. Holben, D. Tanré, and D. E. Ward. 1994. Remote sensing of biomass burning in the Amazon. *Rem. Sens. Rev.*, 10, 51–90.

Mazurek, M. A., W. R. Cofer, and J. S. Levine. 1991. Carbonaceous aerosols from prescribed burning of a boreal forest. In *Biomass Burning: Atmospheric, Climatic and Biospheric Implications*, edited by J. S. Levine, Cambridge, Mass., MIT Press, pp. 258–263.

Patterson, E. M., and C. K. McMahon. 1984. Absorption characteristics of forest fire particulate matter. *Atmos. Environ.*, 18, 2541–2551.

Pyne, S. 1984. *Introduction to Wildland Fire: Fire Management in the United States*. New York, John Wiley, pp. 1–34.

Radke, L. F., S. K. Domonkos, and P. V. Hobbs. 1981. A cloud condensation nucleus spectrometer designed for airborne measurements. *J. Rech. Atmos.*, 15, 225–229.

Radke, L. F., D. A. Hegg, J. H. Lyons, C. A. Brock, P. V. Hobbs, R. Weiss, and R. Rasmussen. 1988. Airborne measurements on smoke from biomass burning. In *Aerosols and Climate*, edited by P. V. Hobbs and M. P. McCormick, A. Deepak Publishing, pp. 411–422.

Ross, J. L., A. P. Waggoner, P. V. Hobbs, and R. F. Ferek. 1996. Airborne lidar measurements of a smoke plume produced by a controlled burn of crude oil on the ocean. *J. Air Waste Manage. Assoc.*, 46, 327–334.

Sandberg, D. V., and J. Peterson. 1984. A source strength model for prescribed fires in coniferous logging slash. In *Proceedings of the 21st Annual Meeting of the Air Pollution Control Association*, Nov. 12–14, Pittsburgh, Penn.

Warner, J., and S. Twomey. 1967. The production of cloud nuclei by cane fires and the effect on cloud droplet concentration. *J. Atmos. Sci.*, 24, 704–706.

Weiss, R. E., V. N. Kapustin, and P. V. Hobbs. 1992. Chain aggregate aerosols in the smoke from the Kuwait oil fires. *J. Geophys. Res.*, 97, 14527–14531.